

## Supplementary material:

### Bubble dynamics in thin liquid film and breakup at drop impact

Elizaveta Ya. Gatapova<sup>1,2\*</sup> and Kyunney B. Gatapova<sup>3</sup>

<sup>1</sup>Kutateladze Institute of Thermophysics SB RAS, Novosibirsk 630090, Russia

<sup>2</sup>Novosibirsk State University, Department of Physics, Novosibirsk 630090, Russia

<sup>3</sup>Moscow Institute of Physics and Technology, Dolgoprudny 141701, Russia

#### *Wettability and roughness of the sapphire plate.*

A sapphire round plate of 40 mm in diameter and 4 mm thick was used as a substrate. Wettability properties were measured using DSA-100E and ADVANCE software (KRÜSS). Advancing contact angle of water on the sapphire plate was measured to be  $CA_{adv}=76.2^\circ$  and receding contact angle –  $CA_{rec}=36.5^\circ$ , so that the contact angle hysteresis was  $CAH=39.5^\circ$  at normal atmospheric condition. Surface free energy was 40.88 mN/m with a disperse component of 34.42 mN/m and polar of 6.46 mN/m, which were measured employing the Owens, Wendt, Rabel, and Kaelble methods using two liquids; polar was water and nonpolar was diiodomethane. Roughness was measured by AFM to be 10 nm.

#### *Setup and experimental data.*

The top view and side view recordings were performed for the same conditions. The top view was organized using the mirror and cold light from the bottom part of the substrate (see Fig. A). Several (at least 7) series of experiments were done for each temperature mode.

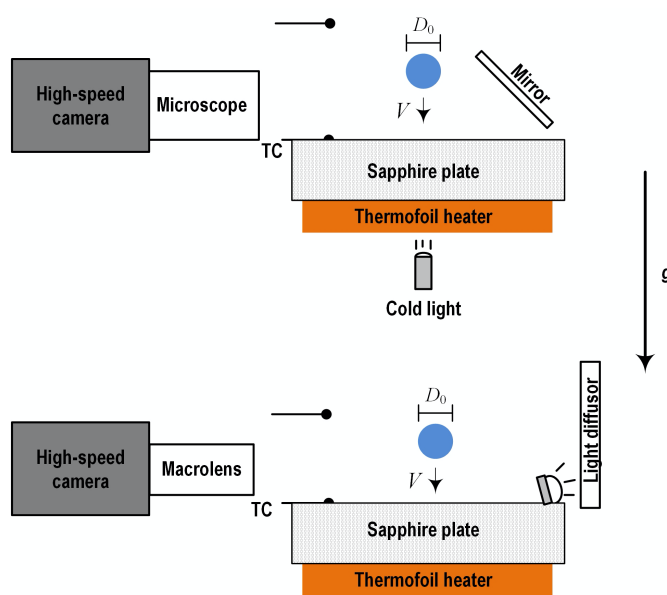


Fig. A. Experimental setup

Characteristic process stages obtained from side view are shown in the supplementary video (side.avi). No liquid column splashing is observed. The rollback is limited and prevented by the thin liquid film breakup. The drop is divided into several sessile microdrops just after the spreading stage. Such division into small droplets is observed also in the work by Sen et al. (2017) for fuel drops. However, the physical reason for the break-up has not been investigated, and no data are available in the literature. In our experiments, these microdrops start boiling and can merge into a single big drop. We observed continuous atomization of microdrops and their levitation during the boiling. With increased temperature, shear interaction of air with drops was becoming substantial. As a result, we observed levitations of the secondary drops (atomized from the main drop) over the substrate, as well as the complete rebounding of the secondary drops. Process stages for the temperature range 23–135°C were discussed in our previous paper [Gatapova et al. (2018)], where liquid film rupture has not been investigated, therefore in the present paper, we focused on the liquid film rupture phenomena and performed special top-view recording experiments for the temperature range 130–170°C.

*Substrate temperature calibration.*

To determine the sapphire plate temperature, the calibration was done using an infrared scanner. Titanium HD 570M (FLIR) infrared scanner with a spatial resolution of 640x512 pixels and frequency up to 115 Hz, and with a minimum resolved temperature difference of the same value as noise (NETD) - 18 mK at 25°C, was used for the substrate temperature calibration. The advantage of the Titanium HD 570M is that it has a spectral range from 3.7 to 4.8 microns, which makes possible to measure water surface temperature, as well as to measure temperature through sapphire substrate. Additional control of the substrate surface temperature was carried out by type-K (Omega) thermocouple, which was connected to the analog input module NL-8TI (RealLab) and interface converter NL-232C (RealLab).

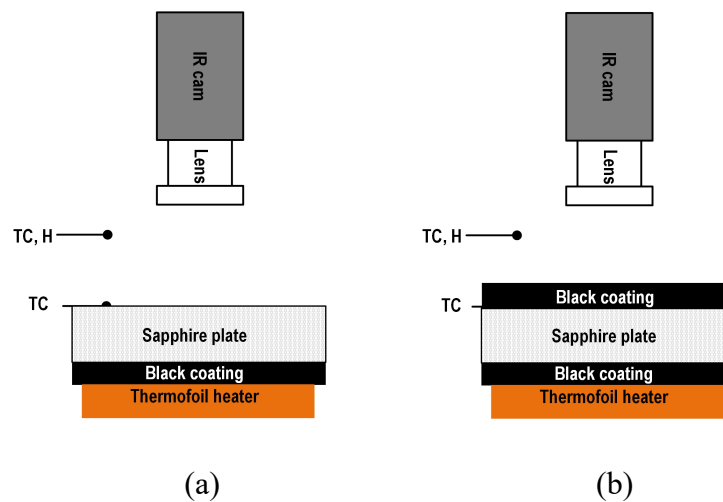


Fig B. The IR calibration of the substrate temperature

Fig. B demonstrates the way for the substrate temperature calibration. First, graphitic conductive black coating (with approximate thickness of 1–3 microns) was deposited at the bottom part of the sapphire plate, and IR measurements were done from the top view through the plate, Fig. B(a). Then the same black coating was deposited on the upper part of the plate, and IR

measurements were done for the upper surface, Fig. B(b). The accuracy of the IR measurements was 0.1K. However, we indicate an average value of the temperature in the middle circle area with a diameter of 20 mm of the substrate (Fig. C). In this area, the temperature varies within  $\pm 1$ K. Air temperature and humidity were controlled by Testo 645 device with an accuracy of 0.1°C and 2%, respectively. Surrounding air temperature and humidity were measured to be 22.8–25°C, and 49–51%, respectively.

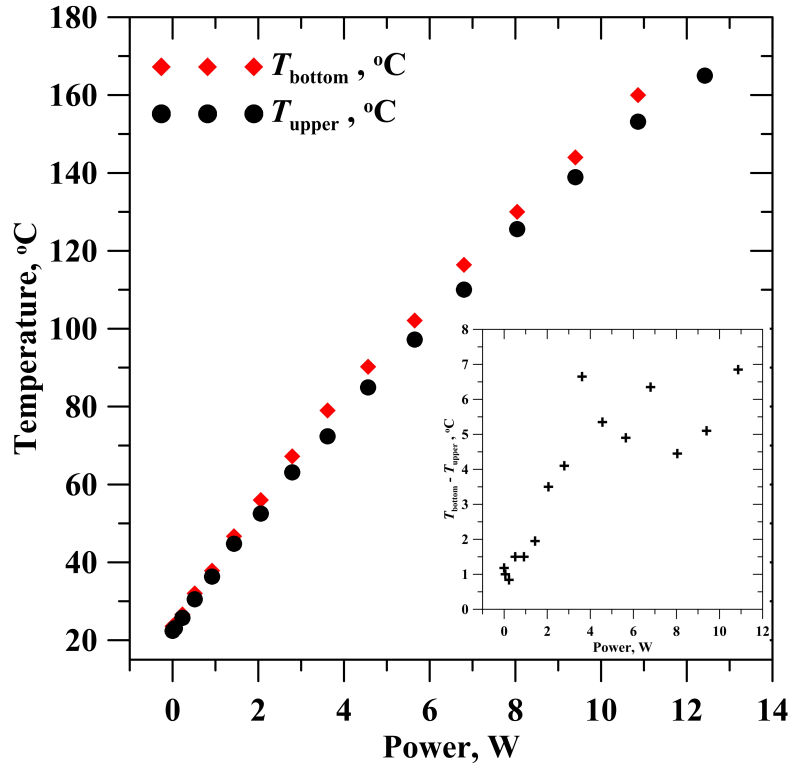


Fig. C. Temperature of the sapphire plate from the top and bottom side versus power. Insertion: the temperature difference between the upper and bottom parts of the plate.

#### *IR recording of the droplet temperature.*

The same Titanium HD 570M IR scanner was used to measure the temperature field of the liquid surface. For such measurements, the sapphire surface was coated by black coating, whose emissivity was about 0.95. The contact angle and hysteresis do not change dramatically when the surface is coated. By IR-recording we can estimate the temperature on the periphery of the expanding droplet, where bubbles form. Fig. D demonstrates IR images at different time for substrate temperature 132 °C. Periphery of the lamella in green temperature zone, about 106 – 108 °C. Figure 12 (in the manuscript) was done using this IR data. One can see the capillary ridge rollback motion, the surface temperature of which in the blue temperature zone (slightly above 100 °C, see also Figure 12 in the manuscript). Fig. E shows the temperature profiles of droplet and substrate surfaces measured by IR-scanner at different time for  $T_w=161$  °C (profiles for half of the droplet).

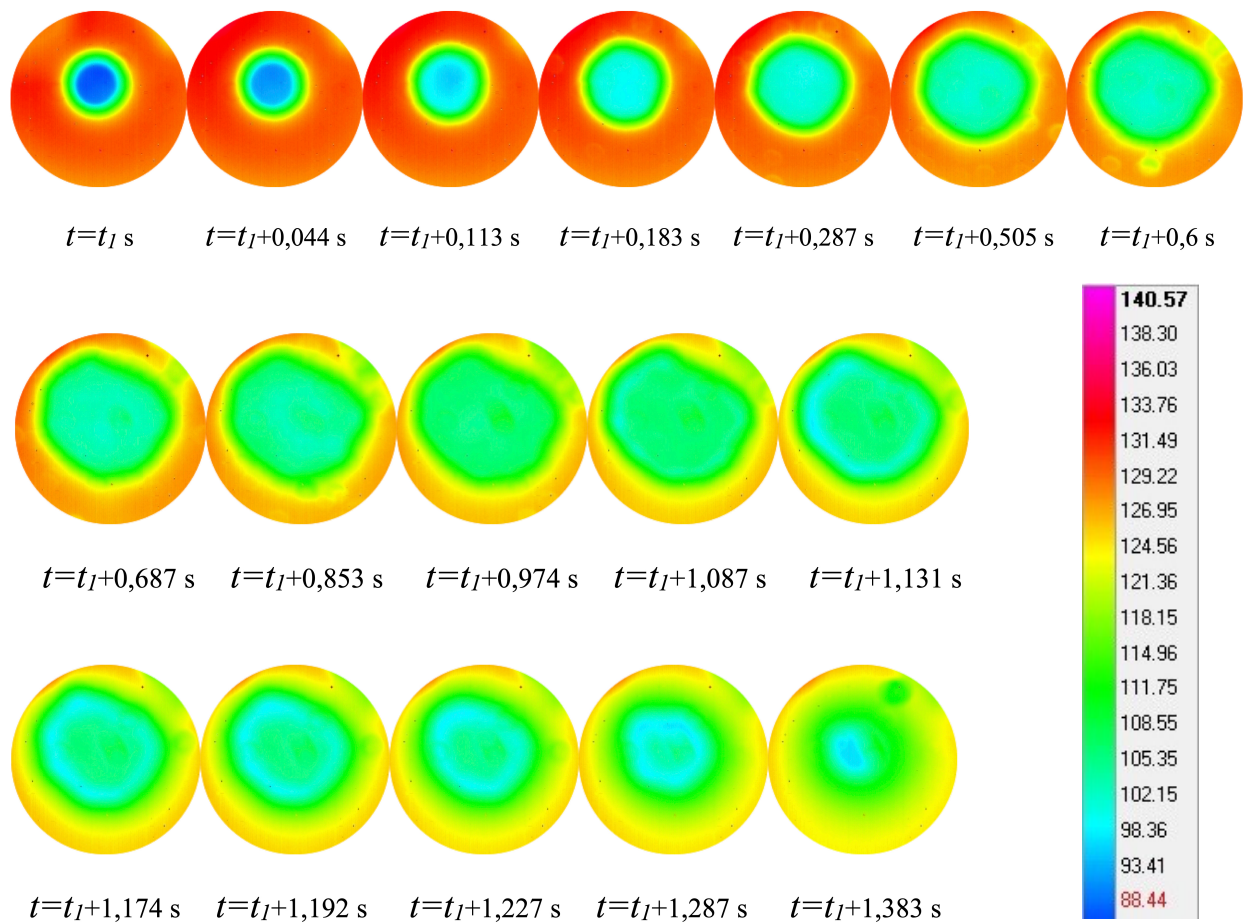


Fig. D. IR images at different time for substrate temperature 132 °C.

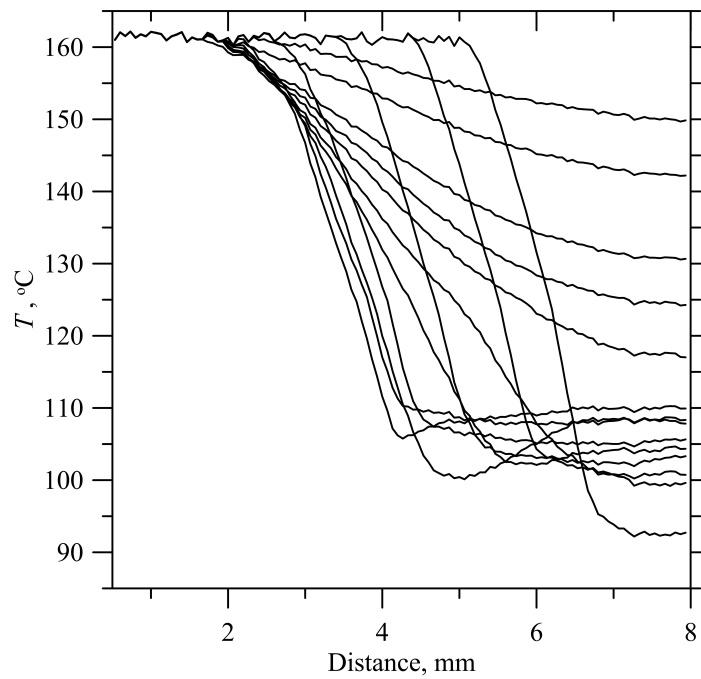
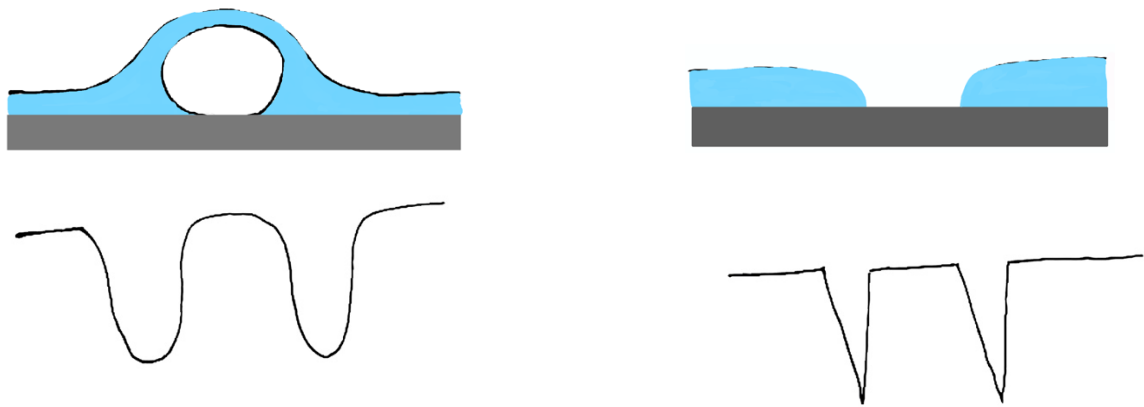


Fig. E. Temperature profiles of droplet and substrate surfaces measured by IR-scanner at different time from initial impact  $t = t_I$  s to  $t = t_I + 1.581$  s for  $T_w = 161$  °C, profiles for half of the droplet.

### Dry patch recognition by ImageJ.

As a first attempt, the playback processing should be done with the indication of irreversible hole formation followed by the dry patch propagation, which helps to recognize the irreversible dry spot formation. Then, more careful processing using the ImageJ software should be done. Schematically, this is illustrated in Fig. F, and the typical picture is presented in Figures G, H.

Figures demonstrate the correspondence of the object and its profiles to gray values. As a rule, the change in gray value (from liquid to the bubble center and dryout region) significantly differs: Bubble (Fig. G) has a flatter transition along the gray value in comparison with the dry patch (Fig. H). This is also due to solid-liquid-gas contact line formation with relatively large apparent contact angle in the case of a dry patch. Additionally, in most cases, the dry region has a relatively long portion of the maximal gray value. We note that enhancing the lateral resolution of images will increase the quality of identification.



(a) Nucleated bubble and its profile gray value (b) Dry patch and its profile gray value

Figure F. Sketch of the typical correspondence between an object and its profile gray value.

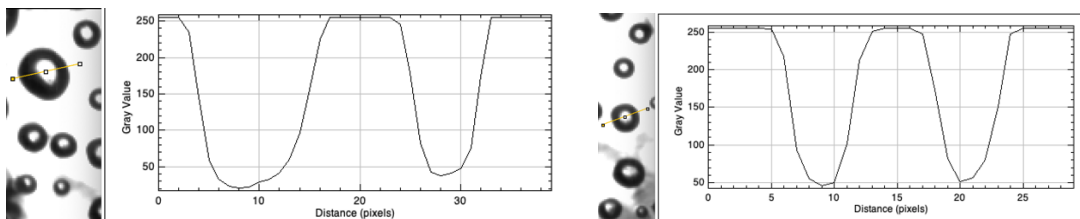


Figure G. Typical gray value profiles of nucleated bubbles (processing in ImageJ).

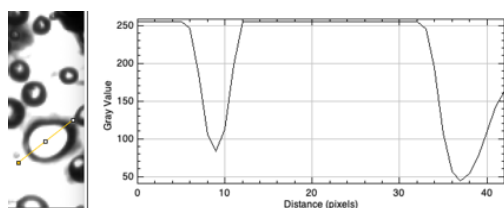


Figure H. Typical gray value profile at the first moment of the dry patch formation (processing in ImageJ).

*Derivation of Equation 3.*

A sketch of the problem under consideration can be found in Fig 7 of the paper. Governing equations are:

$$\mu u_{yy} = p_x \quad (1) \text{ in the liquid film}$$

$$\mu^v u_{yy}^v = p_x^v \quad (2) \text{ in gas/vapor bubbles}$$

The boundary conditions at the vapor–liquid interface:

$$\mu u_y(\delta) = \mu^v u_y^v(\delta) \quad (3)$$

$$u(\delta) = u^v(\delta) \quad (4)$$

At the bottom substrate:

$$u^v(0) = 0 \quad (5)$$

And upper liquid surface:

$$u_y(h) = 0 \quad (6)$$

The solution to this problem gives velocities in liquid and gas phases:

$$u(y) = u(\delta) - \frac{p_x}{\mu} \left( h(y - \delta) - \frac{y^2 - \delta^2}{2} \right) \quad (7)$$

$$u^v(y) = u_y^v(\delta) - \frac{p_x^v}{\mu} \left( \delta y - \frac{y^2}{2} \right) \quad (8)$$

The flow inside the bubble is a gas re-circulation without any gas leakage out of the bubble, so that flow rate inside a bubble is as follows:

$$Q_v = \int_0^\delta u^v dy = 0 \quad (9)$$

Boundary conditions at interfaces (3) and the condition (9) give:

$$u(\delta) = \frac{1}{6} \frac{p_x^v \delta^2}{\mu^v} \quad (10)$$

$$u_y(\delta) = \frac{2}{3} \frac{p_x^v \delta}{\mu} \quad (11)$$

$$\frac{2}{3} p_x^v \delta = -p_x (h - \delta) \quad (12)$$

In the absence of bubbles, liquid flow rate is presented by the well-known formula:

$$Q_l^0 = \int_0^h \frac{p_x}{\mu} y \left( \frac{y}{2} - h \right) dy = -\frac{p_x h^3}{3\mu} \quad (13)$$

Denoting the ratio of bubble size to film thickness by  $K = \delta/h$  the liquid velocity at the liquid-vapor interface and flow rate can be written as follows:

$$u(\delta) = -\frac{1}{4} \frac{h^2}{\mu^v} p_x (1 - K) K \quad (14)$$

$$Q_l = \int_{\delta}^h u dy = -\frac{p_x h^3}{3\mu} (1 - K)^2 \left(1 + \left(\frac{3}{4M} - 1\right) K\right) = Q_l^0 (1 - K)^2 \left(1 + \left(\frac{3}{4M} - 1\right) K\right) \quad (15)$$

where  $M = \mu^v/\mu$  is the ratio between vapor and liquid viscosities.

#### *References:*

Sen S., Vaikuntanathan V., and Sivakumar D., International Journal of Thermal Sciences, 121, 99 (2017).

Gatapova E.Ya., Kirichenko E.O., Bai B., and Kabov O.A., Interfacial Phenomena and Heat Transfer, 6, 75 (2018).

#### *Supplementary video:*

- side.avi – side-view video for substrate temperature of 135°C.
- top135.avi shows the top view recordings for the substrate temperature of 135°C.
- top168.avi shows the top view recordings for the substrate temperature of 168°C.